RSC Advances

ROYAL SOCIETY OF CHEMISTRY

PAPER

View Article Online
View Journal | View Issue

Check for updates

Cite this: *RSC Adv.*, 2026, **16**, 7189

Electrospun PAN + CALF-20 fibers: characterization and removal of Pb(II) and Cu(II) ions from aqueous solution

Guilherme H. F. Melo,[a] Yuxin Liu,[a] Jinfeng Zhang,[a] Nicholas Fylstra,[a] George K. H. Shimizu[b] and Uttandaraman Sundararaj*[a]

This work presents the first report of integrating the Zn-based metal–organic framework (MOF), CALF-20, into electrospun polyacrylonitrile (PAN) nanofibers for wastewater treatment. CALF-20, previously explored for CO_2 capture, is applied here for the first time in fiber-based composite form manufactured *via* direct electrospinning, with MOF loadings ranging from 0 to 70 wt%. These resulting mats are promising for Pb(II) and Cu(II) removal. The PAN + CALF-20 mats, which have uniform morphology, were systematically characterized. They showed good mechanical integrity (up to 60 wt% CALF-20) and high removal capacities for Pb(II) and Cu(II) ions from aqueous solutions, 248.3 mg g^{-1} and 128.2 mg g^{-1}, respectively. Structural analyses (SEM, XRD, and FTIR) confirmed that the dominant removal mechanism is not adsorption but surface-induced precipitation, with distinct crystalline phases forming post-treatment. These results introduce a novel and scalable platform for heavy metal remediation using electrospun MOF-based composites and establish PAN + CALF-20 mat as a promising candidate for multifunctional environmental applications.

Received 10th December 2025
Accepted 23rd January 2026

DOI: 10.1039/d5ra09555g

rsc.li/rsc-advances

1 Introduction

Water pollution has become one of the most significant environmental issues worldwide, affecting aquatic ecosystems, human health, and industrial activities.[1,2] The contamination of water bodies can be categorized into different types, including organic pollution, biological pollution, radioactive contamination, and heavy metal pollution.[1,2] Among these, heavy metal pollution has the most significant health risks due to the toxic and non-biodegradable nature of metal ions such as lead, copper, mercury, cadmium, *etc.*[3]

Lead and copper ions are of particular concern in water pollution.[4] Lead exposure affects the nervous system, particularly in children, and leads to developmental impairments. It is estimated that lead exposure accounts for 0.9 million deaths per year.[5] Copper, although an essential trace ion, becomes harmful when present in high concentrations, leading to liver and kidney damage in humans.[5] The World Health Organization (WHO), in the 4th edition of the Guidelines for Drinking-Water Quality, has set the maximum contaminant level of lead and copper ions in drinking water at 0.01 mg L^{-1} and 2.00 mg L^{-1}, respectively.[6] These strict limits highlight the urgent need for effective water treatment strategies to remove metal ions from contaminated sources.

S. Wei *et al.* presented that, globally, the median of Pb contamination in inland water is 5.81×10^{-3} mg L^{-1}. However, this value changes according to the type of inland water and use of land, with values up to 2.220 mg L^{-1}. Regarding the type of inland water, the Pb concentration was higher in rivers (estimated mean of 1.656 mg L^{-1}). Within the use of land, industrial, residential, and agricultural lands showed similar mean values (2.405, 2.346, and 2.335 mg L^{-1}, respectively).[7] The concentration of copper also varies according to the type of water analyzed, in tap water the average concentration varies from 2.0×10^{-2} to 7.5×10^{-2} mg L^{-1}, the concentration in rivers and lakes ranges from 5.0×10^{-4} to 1.0 mg L^{-1}, with some groundwater presenting up to 2.80 mg L^{-1}.[8]

Several methods have been employed to tackle heavy metal pollution in water, such as chemical precipitation, ion exchange, membrane filtration, and adsorption.[9] Among these, adsorption is favored due to its simplicity, efficiency, and cost-effectiveness [10]. Adsorbents such as activated carbon, zeolites, and more recently, metal–organic frameworks (MOFs) have gained significant attention for this purpose due to its ease of synthesis, structure tunability, possibility of chemical modification, aligned with many different mechanisms of removal.[11,12]

MOFs are a class of porous coordination polymers composed of metal ions or clusters coordinated to organic ligands, forming extended networks.[13] The potentially tunable structures, large surface areas with unique electronic properties, and

---

[a] Department of Chemical and Petroleum Engineering, University of Calgary, 2500 University Dr NW, Calgary, AB T2N 1N4, Canada. E-mail: guilherme.melo@ucalgary.ca; ut@ucalgary.ca

[b] Department of Chemistry, University of Calgary, 2500 University Dr NW, Calgary, AB T2N 1N4, Canada

structural void volumes make them ideal candidates for adsorption-based applications.[14] For example, MOFs like NU-1000, TMU-4, ZIF-67, and ZIF-8 have shown excellent ability to remove both copper and lead from water.[11,15–17] Y. Huang *et al.* showed that the adsorption capacity of ZIF-8 and ZIF-67 for Pb(II) reach 1119.80 and 1348.42 mg g^{-1}, and for Cu(II) 454.72 and 617.51 mg g^{-1}, respectively.[18]

Although numerous studies have explored the use of MOFs for heavy metal adsorption, ongoing research is still needed. This is because many current MOF structures suffer from high synthesis costs, limited stability under real-world conditions, and challenges in large-scale production,[19] which hinder their practical application in environmental remediation. Calgary Framework 20 (CALF-20), a relative new MOF, has gained attention due to its green, simple, and industrial scalable synthesis process, as well as its stability and versatility. In 2014, the Shimizu group at the University of Calgary reported the Zn-based MOF named CALF-20, which consists of repeating layers of 1,2,4-triazoles connected by Zn atoms with oxalate ions bridging the layers forming a 3D lattice and pore structure,[20] resulting in structures with surface area in the order of 550 m^2 g^{-1}.[21] CALF-20 demonstrates an excellent CO_2 adsorption capacity of 4.07 mmol g^{-1} at 1.2 bar and 293 K, CO_2 selectivity against water at up to 60% relative humidity, and provides durability and stability to steam, wet acid gases, and can withstand prolonged exposure to direct flue gas stream.[21] Moreover, CALF-20 is very promising commercially since its production yields up to 90% and shows an exceptional space-time yield of 550 kg m^{-3} per day.[21]

Despite the wide-ranging potential applications and desirable properties of MOFs, one of their main limitations is that the final product is typically obtained as a powder,[22,23] which cannot be easily sintered or molded into specific shapes due to its lower thermal stability compared to Zeolites[6] (CALF-20 degrades around 350 °C[24] and the zeolite 13× degrades at temperatures higher than 800 °C[25]), meaning that using MOFs as powders alone presents practical challenges in water treatment applications. The powder is difficult to process, leading to issues such as agglomeration, heterogeneity, pressure drop, and material loss during the process.[11] To overcome these limitations, researchers have explored incorporating MOFs into polymer nanocomposites, specifically by immobilizing MOFs onto polymeric nanofibers to create a structured form.[26] These nanofibers not only provide a flexible substrate but also retain a significant portion of the MOFs' high surface area, efficient metal removal provided by the content of the MOF in the polymer can be achieved at sufficiently high loading.[27] Additionally, they offer the advantage of being easier to handle and integrate into water treatment systems.[26]

Polyacrylonitrile (PAN) has been employed in this study as the polymer matrix due to its excellent spinnability, chemical stability, and compatibility with MOF incorporation. Previous studies have demonstrated that electrospun nanofiber mats composed of PAN exhibit high affinity toward heavy metal ions, supporting the potential of such fibrous materials in water purification technologies.[28,29] The integration of CALF-20 into the PAN-based electrospun fibers aims to synergistically combine the high surface area and porosity of CALF-20 with the tunable functionalities of nanofibrous membranes. This study is the first to integrate CALF-20 into electrospun nanofibers and shows its potential for Pb(II) and Cu(II) removal. The resulting nanofibers were thoroughly characterized using scanning electron microscopy (SEM), X-ray diffraction (XRD), Fourier-transform infrared spectroscopy (FTIR), and X-ray photoelectron spectroscopy (XPS) to confirm successful incorporation of CALF-20 and to analyze the morphological, structural, and chemical features. Additionally, adsorption performance for Pb(II) and Cu(II) was evaluated through isotherm and kinetic modeling, providing mechanistic insights into the interaction between metal ions and the PAN + CALF-20 electrospun fibers.

2 Materials and methods

2.1 CALF-20 synthesis

To synthesize small particles of CALF-20, a modified method was employed. First, 95% ethanol (VWR Chemicals) was heated to its boiling point (∼85 °C) in a round-bottom flask apparatus with a water-cooled condenser. Zinc carbonate was then gradually added while stirring the flask contents. In parallel, a Pre-CALF-20 adduct solution was prepared by dissolving 1,2,4-triazole (Sigma-Aldrich >97.0%) and oxalic acid dihydrate (Honeywell™ Fluka™ >99.99%) in ethanol, followed by sonication for 30 minutes to ensure thorough mixing, then it was added to the zinc carbonate solution.[30] The molarity zinc carbonate, oxalic acid, and 1,2,4-triazole was 0.65, 0.65, and 1.10 M, respectively.

2.2 CALF-20 + PAN fibers preparation

PAN nanofibers containing CALF-20 particles were made through direct electrospinning. The solution preparation scheme is shown in Fig. 1a. First, a certain amount of CALF-20 was added to 5 mL of a mixture of DMF (Fisher Chemical >99.8%) and acetone (VWR Chemicals > 99.8%) (4 : 1 v/v). Then, the mixture was sonicated for 20 minutes to disperse the MOF particles. After this period, 0.50 g of PAN (Zhonghui Co. LTD M_w = 150 000 g mol^{-1}) was added, and the mixture was stirred at 30 °C for 1 h. Finally, the solution was electrospun for 3.5 hours using 13 kV of applied voltage, collector speed of 600 rpm, solution flow rate of 1.000 mL h^{-1}, 6 cm distance of the needle to the collector, chamber temperature varying of 22–23 °C, and relative humidity from 11 to 12% (Fig. 1b).

The weight percentage of CALF-20 in PAN varied from 0 to 70 wt% at 10 wt% increments, and the amount of material used for each sample is detailed in Table 1. The amount of PAN, acetone and DMF were kept constant while the amount of CALF-20 was changed.

2.3 Batch Cu(II) and Pb(II) removal

The removal experiments of Cu(II) removal from water solution were carried out by using a constant mass (m = 0.1 g) of electrospun mat that was immersed in a volume (V_0 = 0.1 L) of an aqueous solution containing copper nitrate hexahydrate ($Cu(NO_3)_2 \cdot 6H_2O$) (Sigma-Aldrich >99.0%) with an initial Cu(II)

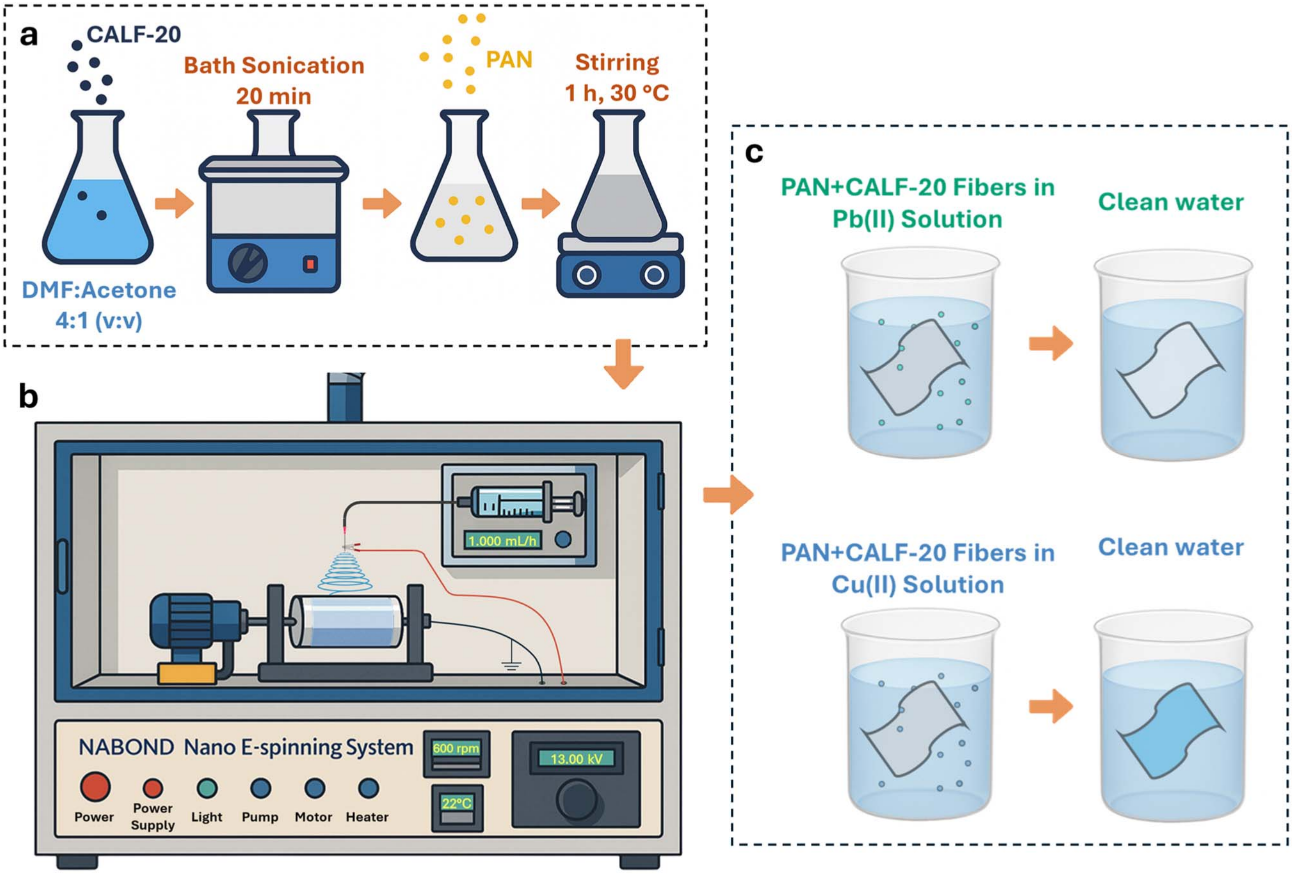

Fig. 1 Schematic representation of the: (a) solution preparation, (b) electrospinning process and (c) the metal removal.

Table 1 Amount of material used in each sample for the electrospinning solution

CALF-20 (wt%)	CALF-20 (g)	PAN (g)	Acetone (mL)	DMF (mL)
0	–	0.5	1	4
10	0.055	0.5	1	4
20	0.125	0.5	1	4
30	0.215	0.5	1	4
40	0.333	0.5	1	4
50	0.500	0.5	1	4
60	0.750	0.5	1	4
70	1.166	0.5	1	4

concentration (C_0) varying from 50 to 400 mg L^{-1} at pH 6.5. The solution was stirred at 450 rpm at 22 °C. The evaluation of Pb(II) adsorption was performed by immersing 0.05 g of electrospun mat in 0.1 L of an aqueous solution containing lead nitrate ($Pb(NO_3)_2$) (Sigma-Aldrich >99.0%) with initial Pb(II) concentration varying from 50 to 600 mg L^{-1}, at pH 6.5, 22 °C, and stirred at 450 rpm. The initial metal concentration was chosen to be above everyday values to find maximum removal values under saturated conditions, as well as to provide better data for the study of isothermal models. The influence of pH, the membrane loading and initial metal concentration were performed with pH from 3 to 6.5, membrane loading from 0.5 to 1.5 g L^{-1}, and initial metal concentration from 50 to 200 mg L^{-1}. Subsequently, the removal capacities at a different time (q_t) were calculated using eqn (1), where the ion concentration obtained at each time (C_t) is measured by ICP-OES. The removal efficiency ($R\%$) was calculated using eqn (2).[31]

$$q_t = \frac{V_0(C_0 - C_t)}{m} \tag{1}$$

$$R\% = 100\%\left(\frac{1 - C_t}{C_0}\right) \tag{2}$$

2.4 Kinetic and isotherm models

To study the kinetics of removal, the data was compared with the pseudo-first and pseudo-second order models (PFO and PSO, respectively), represented by the eqn (3) and (4).[32]

$$q_t = q_e(1{-}e^{-kt}) \tag{3}$$

$$q_t = \frac{k{q_e}^2 t}{1 + kq_e t} \tag{4}$$

where q_e is the equilibrium removal capacity and k is the rate constant.

The models used to evaluate the isotherms were Langmuir Freundlich,[60] and Temkin, [61] represented by the eqn (5)–(7).

$$q_e = \frac{q_m K_L C_e}{1 + K_L C_e} \tag{5}$$

$$q_e = K_F C_e^{1/n} \tag{6}$$

$$q_e = \frac{RT}{b_{\mathrm{T}}}\ln(K_{\mathrm{T}}C_e) \tag{7}$$

where q_m is the maximum removal capacity, C_e is the concentration of heavy metal ion in solution at equilibrium and K_{L} is the Langmuir adsorption constant, K_{F} = Freundlich isotherm constant, n = adsorption intensity, K_{T} = Temkin isotherm equilibrium binding constant, b_{T} = Temkin isotherm constant, T = temperature (K), R = universal gas constant [8.314 J mol^{-1} K^{-1}].[33–35]

2.5 Characterization

The morphologies of the samples were analyzed by a Scanning Electron Microscope (SEM) Zeiss SIGMA VP (Oberkochen, Baden-Württemberg, Germany). To evaluate the mechanical properties of the electrospun mats, 5 samples of each condition were cut in a dogbone shape (ASTM D638)[36] and subjected to a tensile strength test performed at room temperature (22–23 °C) by an INSTRON 5965 dual column tabletop testing system at a rate of 5.00 mm min^{-1} as per ASTM D638. The fiber diameter was measured using ImageJ software version 1.54k15, and the final value was obtained after taking the average and standard deviation of 100 measurements. For the surface area and pore size distribution, N_2 sorption analyses were conducted *via* a Micromeritics TriStar II 3020 Surface Area and Porosity Analyzer (Norcross, Georgia, USA) at 77 K, the samples were activated under vacuum at 393 K for 12 hours. The powder X-ray diffraction (PXRD) patterns of the samples were obtained using a Bruker D8 Advance (ECO) (Billerica, Massachusetts, USA) diffractometer operating in the range of 2θ from 5° to 40° with CuKα radiation (λ = 1.5406 Å). The infrared spectra of the samples were performed by an Agilent Cary 630 Fourier-transform infrared spectroscope (FTIR) (Santa Clara, California, USA) with a resolution of 2 cm^{-1} from 400 to 4000 cm^{-1} wavelength. The heavy metal removal characterization was performed by Inductively Coupled Plasma Optical Emission Spectroscopy (ICP-OES) using the equipment iCAP 7200 (Waltham, Massachusetts, USA). The X-ray Photoelectron Spectroscopy (XPS) was performed using a Thermo-Fisher ESCALAB QXi XPS Microprobe (Waltham, Massachusetts, USA).

3 Results and discussion

3.1 Electrospun fibers

The mats obtained in the electrospinning process showed good mechanical condition, since they were easily removed from the collector (without damage) and easily handled (Fig. S1). The morphological evaluation (fiber diameter distribution and MOF particles size) was performed by SEM. Compared to C, N, O, and H (elements present in PAN and CALF-20), Zn (only present in CALF-20) has a higher atomic number, which makes it possible to differentiate polymers and filler through backscattered electron (BSE) microscopy. Fig. 2 shows the SEM images from the BSE detector, where the bright areas are attributed to the presence of CALF-20. All electrospun mats presented a uniform morphology, without the presence of polymer beads or major defects.

The pure PAN mat (Fig. 2a) was very uniform, with smooth fibers and diameters of 400 ± 60 nm and randomly oriented. After adding CALF-20, the fibers were composed of two heterogeneous regions, one without the presence of CALF-20 (only PAN) and the other containing CALF-20 particles. As expected, the area containing CALF-20 is more prevalent as the particle content increases, and CALF-20 particles can be clearly seen in the SEM images at Fig. S2. As we increase to up to 60 wt% CALF-20, the fiber region containing CALF-20 presents a bigger diameter than the area with only PAN due to the particle size (in the order of 1 to 5 μm). However, it did not significantly change the diameter of the PAN fiber, with diameters changing from 265 ± 65 nm to 390 ± 105 nm.

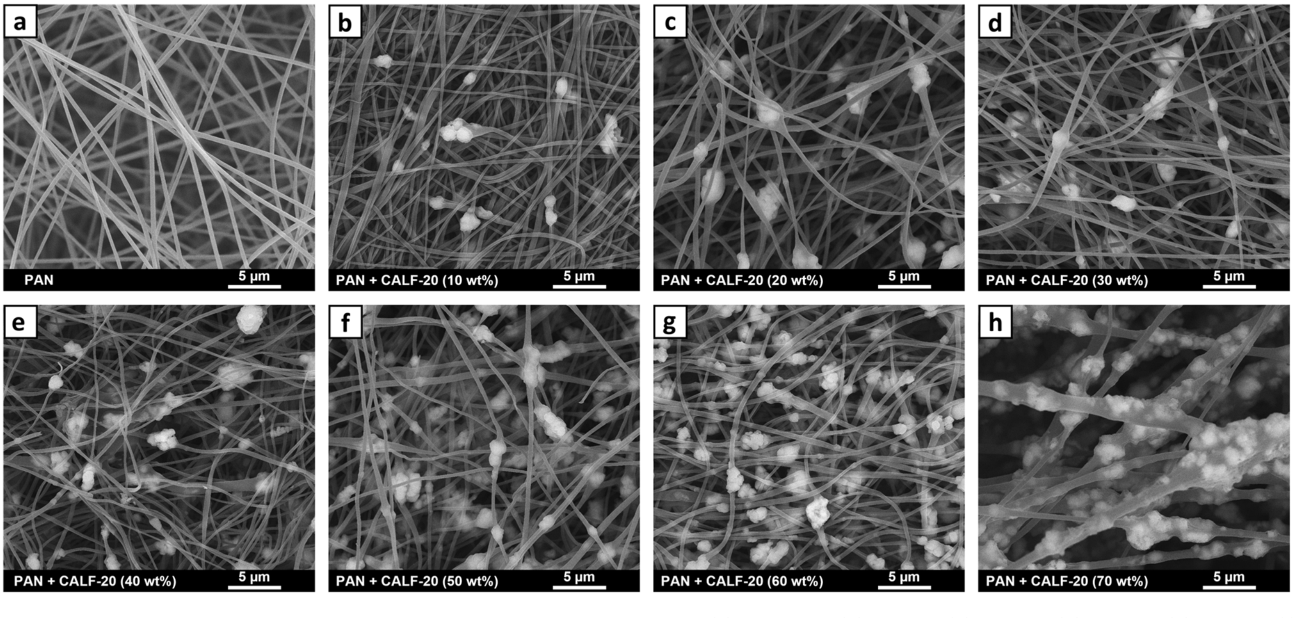

Fig. 2 BSEM images of the electrospun mats with different CALF-20 content. (a) pure PAN, (b) 10 wt%, (c) 20 wt%, (d) 30 wt%, (e) 40 wt%, (f) 50 wt%, (g) 60 wt%, and (h) 70 wt%.

Moreover, at 70 wt% of CALF-20 (Fig. 2h), the fiber diameter increased significantly to 1090 ± 475 nm. This increase is attributed to the higher filler content, which means we have a greater number of dispersed particles, but higher filler content also promotes formation of more agglomerates, ultimately leading to an increase in the average fiber diameter. The distribution of fiber diameters is shown in Fig. S3. Aside from the formation of agglomerates, the MOF particles were very well coated with PAN (Fig. S4).

The stress–strain curves shown in Fig. 3a present two main regions: the first at low deformations with a higher elastic modulus and the second at higher deformations with a lower elastic modulus. This occurs because in the first stage the fibers are relatively aligned, providing greater resistance to deformation. Once the initial stiffness is overcome, additional deformation mechanisms may occur, such as fibers sliding past each other, microfractures, delamination, or fiber pull-out, leading to a softer mechanical response. The addition of CALF-20 content does not significantly interfere with the modulus of each region, but it does interfere where transitions between deformation regions occur. For concentrations between 10 and 30 wt%, the transition occurs at greater deformations, than those for pure PAN. With higher CALF-20 content, the transitions occur at smaller deformations, becoming almost imperceptible in the curve for to 70 wt% CALF-20.

The mechanical properties of the mats at different CALF-20 weight percentages (Fig. 3b) show that the tensile strength (σ) has a maximum value of 8.1 ± 0.9 MPa at a concentration of 10 wt%; at higher CALF-20 loadings, the tensile strength decreases to 0.8 ± 0.3 MPa for mats loaded with 70 wt% of CALF-20 (the lowest value for all composites and 7.5 times smaller than the pure PAN). The elongation at break (ε) followed a similar trend, however, the maximum value was obtained for 40 wt% CALF-20 (0.25 ± 0.05 mm mm^{-1}) and the lowest value for 70 wt% CALF-20 (0.17 ± 0.01 mm mm^{-1}), this is only 1.4 times smaller than mats with pure PAN. This indicates that at low CALF-20 concentrations the particles act as an anchoring point for the fibers and increase mechanical resistance. At concentrations greater than 30 wt%, these particles act as defects that act as initiating points for rupture and thus reducing the mechanical resistance of the mats.

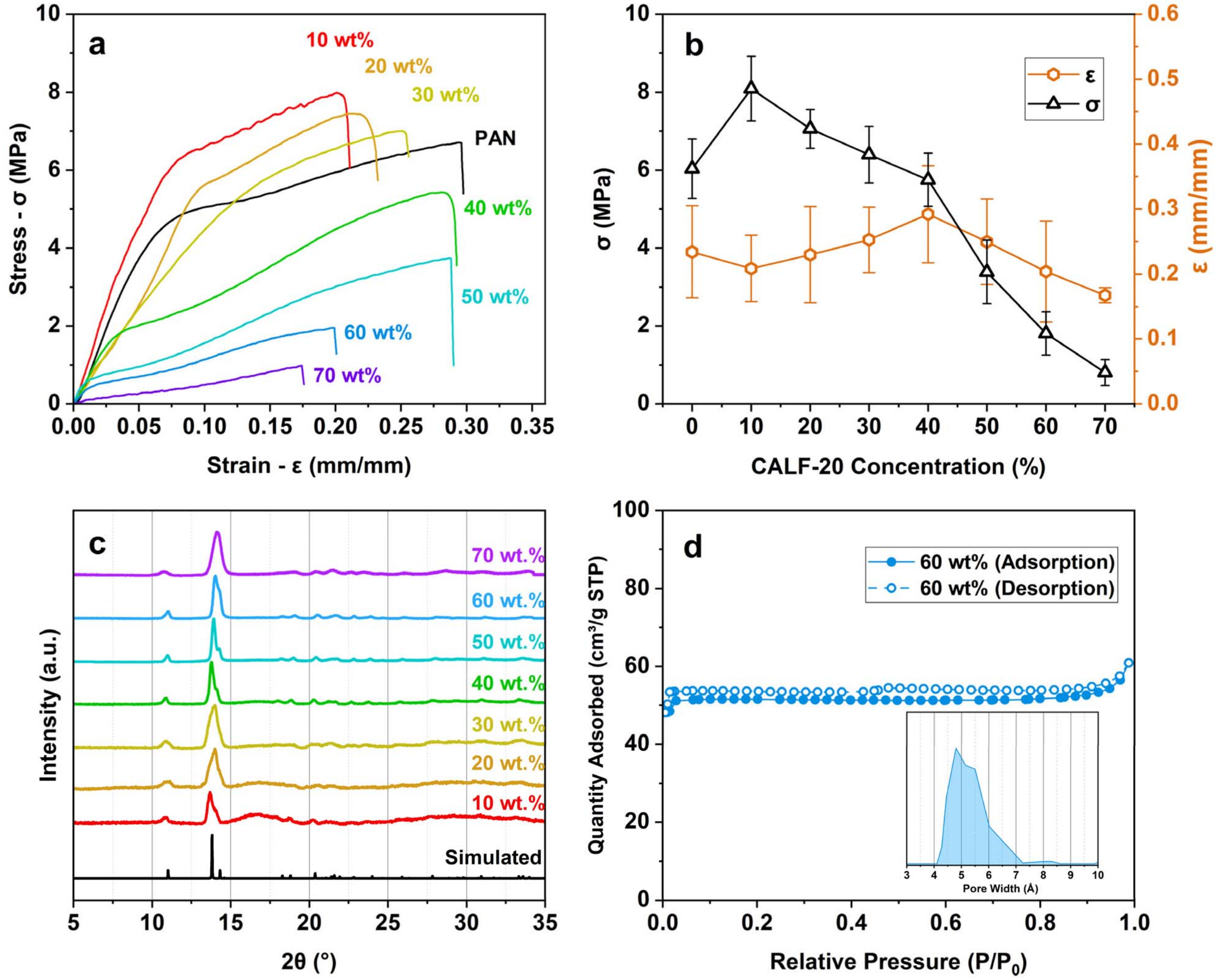

Fig. 3 (a) Stress–strain curves (curve represents the sample with the behavior closest to the average of the 5 samples). (b) Average tensile stress and strain at break. (c) Normalized PXRD patterns (black pattern is simulated CALF-20) of electrospun mats containing different weight percentages of CALF-20. (d) 77 K N_2 isotherm of electrospun CALF-20 (60 wt%) + PAN (inserted pore size distribution).

The XRD patterns, Fig. 3c, show that all samples present the characteristic peaks of CALF-20 (the two peaks around $2\theta = 14°$ are clearly seen), indicating the successful incorporation of CALF-20 in the mats without any phase transformation during the electrospinning process. The 77 K N_2 adsorption–desorption isotherm for the sample containing 60 wt% CALF-20, is shown in Fig. 3d. The curve is a Type I isotherm with a rapid uptake at low partial pressures.[37] Soon after the knee, a slight hysteresis is seen at intermediate pressure regime.

Knowing that the theoretical density and BET surface area of CALF-20 are 1.689 g cm^{-3} (calculated from CIF file)[38] and 555 m^2 g^{-1} (obtained experimentally here), respectively, the estimated surface area for the composite containing 60 wt% ($\approx$48 v%) is 266 m^2 g^{-1}, however, the surface area measured by BET was 161 m^2 g^{-1}. The reduced value is explained by the fact that part of the CALF-20 particles is covered by PAN, obstructing some of the pores.

3.2 Pb(II) and Cu(II) removal

The PAN + CALF-20 mats led to the removal of lead and copper ions present in aqueous solution. When using pure PAN fibers the removal of Pb(II) and Cu(II) is very low, however, when CALF-20 is added the removal kinetics are fast in the first hour, both for the removal of Pb(II) (Fig. 4a) and Cu(II) (Fig. 4b) and the removal capacity increases with increasing the CALF-20 content. It proves that the presence of CALF-20 leads to the removal of Pb(II) and Cu(II) from aqueous solution.

For Pb(II) removal, using 10 wt% of CALF-20, the removal reaches a plateau in 30 minutes at a capacity of $\approx$35 mg g^{-1}, indicating that the material has reached equilibrium and the maximum possible removal capacity under those conditions ($C_0 = 100$ mg L^{-1}, $T = 23$ °C, pH = 6.5, $m = 0.05$ g, and $V_0 = 0.1$ L). However, samples with a higher amount of CALF-20 do not reach complete equilibrium in the 240 minutes of experiment; only the samples containing 60 and 70 wt% show a clear slowdown in the Pb(II) removal process after 120 minutes and are the samples with the highest removal capacity (194.1 and 208.4 mg g^{-1} at 240 minutes), for 60 and 70 wt% respectively.

The Cu(II) removal kinetics showed a similar behavior at slightly different conditions ($C_0 = 135$ mg L^{-1}, $T = 23$ °C, pH = 6.5, $m = 0.10$ g, and $V_0 = 0.1$ L) where there was a rapid removal in the first 60 minutes, followed by a deceleration. At this condition, all samples showed a plateau within the 240 minutes interval for the Cu(II) removal.

The adsorption capacity and removal efficiency (Fig. 4c and d) gradually increase with increasing CALF-20 content, reaching values of 208.4 mg g^{-1} and 96.6% for Pb(II) and 132.9 mg g^{-1} and 99.5% for Cu(II) for 70 wt% of CALF-20. Despite this, after

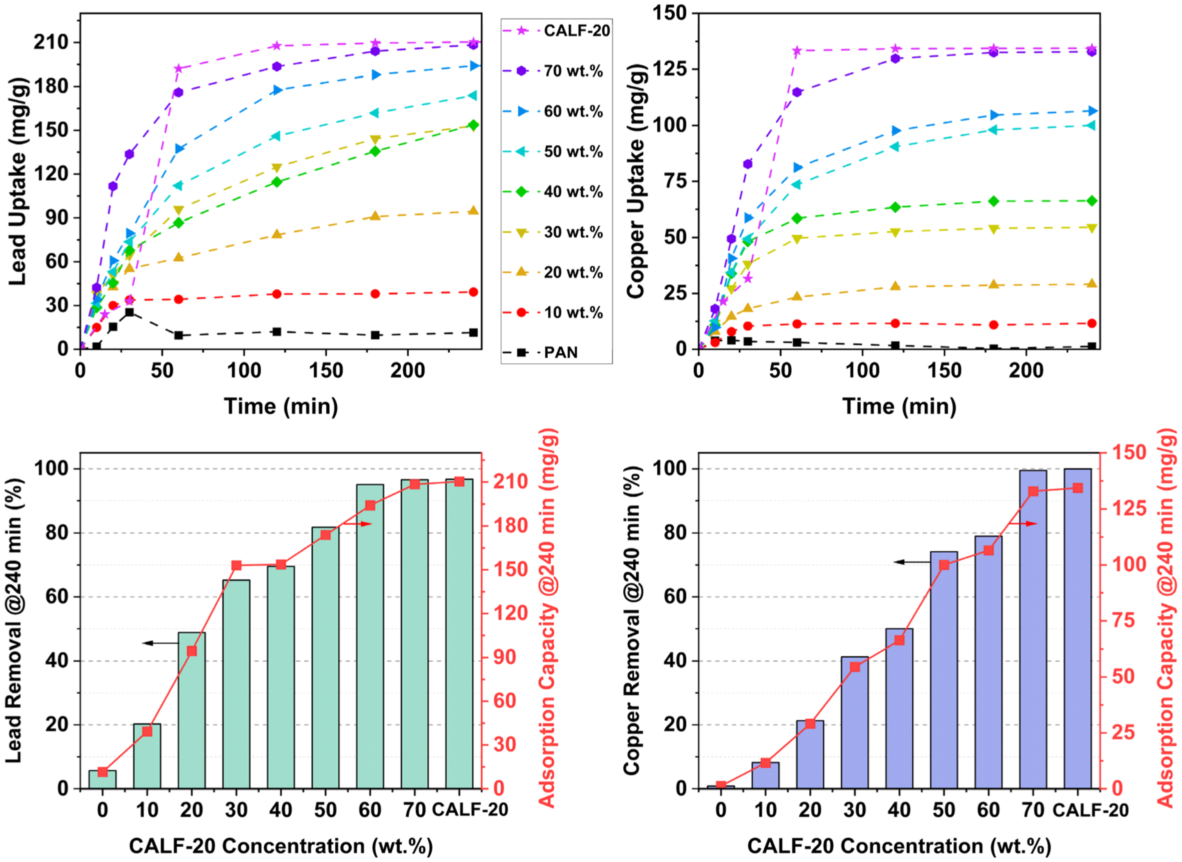

Fig. 4 Removal kinetics of: (top left) Pb(II) and (top rigjht) Cu(II) for electrospun mats containing different weight concentrations of CALF-20 compared with pristine CALF-20. Removal efficiency and adsorption capacity of (bottom left) Pb(II) and (bottom right) Cu(II) @240 minutes for electrospun mats containing different weight percentages of CALF-20 compared with pristine CALF-20. Initial concentration (C_0) 100 mg L^{-1} for Pb(II) and 135 g mL^{-1} for Cu(II).

the removal of Pb(II) or Cu(II) from the aqueous solution, the samples containing 70 wt% of CALF-20 were completely broken into small pieces (Fig. S5) due to their low mechanical properties, as presented in the previous section, which makes reuse of these high concentration mats unfeasible. Mechanical failure not only prevents direct recovery of the membrane after use, but also hinders the separation of treated water, increases the risk of secondary contamination by membrane small pieces, and eliminates the possibility of controlled regeneration. Consequently, the lack of mechanical stability makes repeated use unfeasible, compromising the practical applicability of the membrane, despite its promising performance in removing heavy metals. Thus, the sample containing 60 wt% of CALF-20 is chosen as the best among those studied, as it presents high values of adsorption capacity and removal efficiency (194.1 mg g^{-1} and 95.1% for Pb(II) and 106.5 mg g^{-1} and 79.0% for Cu(II)), and has mechanical integrity after the removal process (Fig. S6 and S7).

It is possible to observe in Fig. 4 that the removal is due to the presence of CALF-20, since the adsorption capacity and removal efficiency are very low when pure PAN fibers are used (10.7 mg g^{-1} and 5.3% for Pb(II); 1.1 mg g^{-1} and 0.8% for Cu(II)).

Additionally, at the same conditions, pristine CALF-20 shows a faster removal kinetics for both copper and lead, reaching the saturation within 60 minutes, besides the slow removal in the beginning of the removal process (between 0 and 30 minutes). Despite the difference in removal kinetics, the final values, both for removal capacity and removal efficiency after 4 hours of removal process, are quite similar to the CALF-20 (70 wt%) + PAN membranes. The kinetics of the composite may be slowed due to the lower accessibility of the CALF-20 particles, while the high removal values can be explained by the presence of more surface area for precipitate deposition, as observed in Fig. 5.

The SEM images (Fig. 5) present the morphological characteristics of the electrospun fiber containing 60 wt% of CALF-20 after Pb(II) and Cu(II) removal from the aqueous solution. Fig. 5a, shows an image of the mat after Pb(II) removal, and displays relatively large, well-faceted crystals with smooth surfaces and two main shapes: hexagonal plates and needle-like. The size distribution of the hexagon plates appears relatively broad, with individual crystals ranging from 0.5 to 10 µm in length. The overall morphology indicates a relatively controlled growth condition, favoring the development of distinct, compact crystalline domains with lead-based coordination or salt compounds. A similar phenomenon was observed by W. Wang *et al.* when the structure of ZIF-8, in the presence of Ga liquid and water, was easily transformed to Zn–Ga 2D layered double hydroxide (LDH) crystal.[39] It shows that the MOF structures might not be completely stable under some environments, leading to changes and formation of secondary products. This information suggests that the CALF-20 present in the fibers got degraded during the Pb(II) removal and formed a different product compound.

In contrast, Fig. 5b of the mat after Cu(II) removal, shows a very different microstructure. The PAN + CALF-20 fibers are heavily coated with bipyramidal particles with approximate size of 0.15 µm. These particles have smooth surfaces, defined edges and three-dimensional shape. These images indicate that the main mechanism of removal is precipitation, instead of adsorption, that might be caused by the nitrate anions.

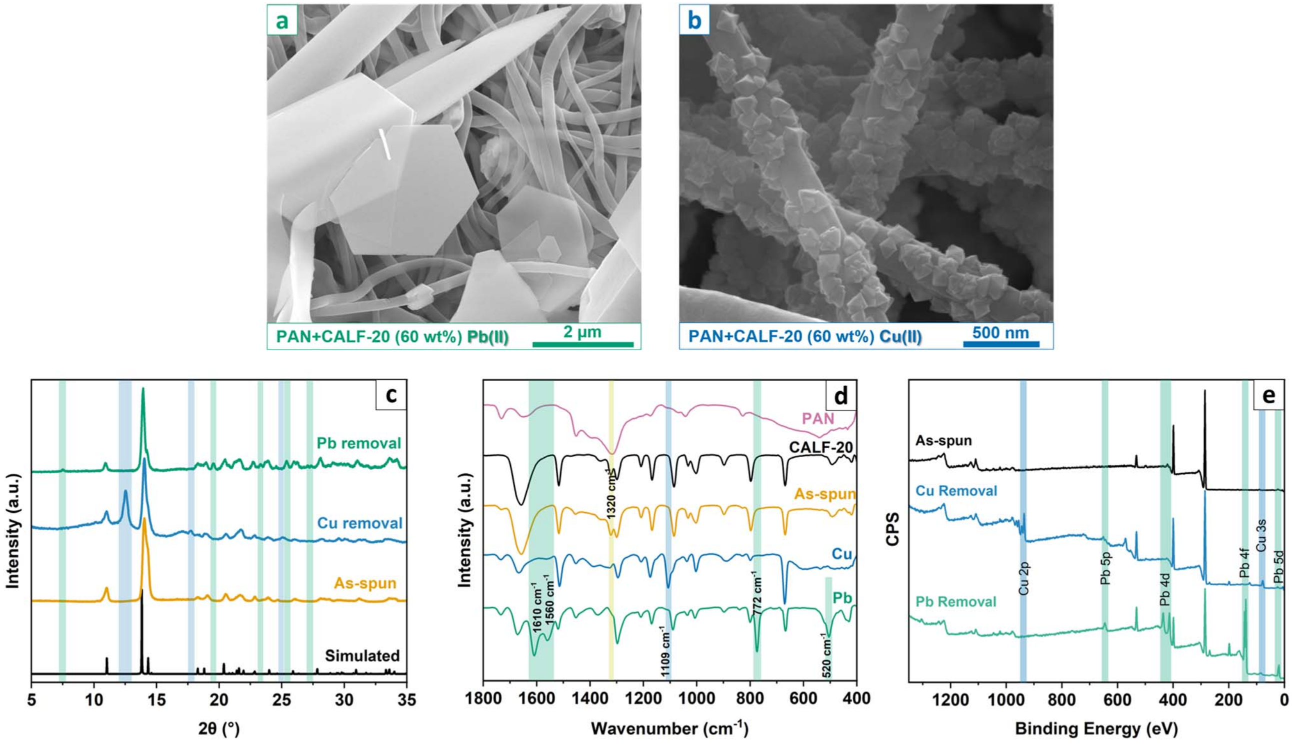

Fig. 5 SEM images of electrospun mats (CALF-20 (60 wt%) + PAN) after removal of: (a) Pb(II), and (b) Cu(II) for 240 minutes. (c) XRD pattern, (d) FTIR spectra, and (e) full XPS spectra of the as-pun mats and after metal removal.

XRD, FTIR and XPS were performed for structural characterization. The XRD diffractogram in Fig. 5c shows the simulated pattern for CALF-20 and experimental result for the 60 wt% CALF-20 as-spun mat, and after Cu(II) and Pb(II) removal. The XRD pattern of the as-spun sample shows all the same peaks as the simulated pattern for CALF-20, the only difference is the peak width, that increase due to the reduced particle size.

In the 13–15° 2θ region (Fig. S8), the simulated CALF-20 XRD pattern exhibits two distinct peaks at 13.8° and 14.3°. The as-spun PAN + CALF-20 (60 wt%) fibers display overlapping peaks with a maximum intensity at 14.0°, a feature that is also observed after Cu(II) removal, indicating that the CALF-20 framework remains structurally intact. In contrast, after Pb(II) removal, the overlapping peaks show a slight shift to 13.9°, suggesting a structural modification. This shift can be attributed to partial ion exchange, where Pb(II) replaces Zn(II) in the framework, with the larger atomic radius of Pb(II) causing the observed reduction in the peak angle. The overlapping nature of the experimental peaks is likely due to particle size effects and the adsorption of guest molecules, such as CO_2.[40] However, after Pb(II) removal, it is possible to observe the presence of very small new peaks at $2\theta = 7.5$, 19.5, 23.3, 25.4, 27.0, and 27.3°. The XRD pattern of the sample after Cu(II) removal shows new peaks at $2\theta = 12.5$, 17.7, and 25.0° which can be attributed to the formation of copper hydroxy nitrate ($Cu_2(OH)_3NO_3$).[41,42]

Based on particles shape seen in the SEM image, and XRD pattern, combined with nitrate-rich adsorption experiment conditions, the predominant product is proposed to be copper complex. This basic salt typically forms under mildly alkaline conditions in the presence of nitrate ions, suggesting that a local chemical environment was created by the CALF-20 + PAN membrane and facilitated a controlled crystallization of copper-based phases. The proposed mechanism, catalysed by CALF-20, is described by:

$$2Cu^{2+} + 4NO_3^- + 3H_2O \rightarrow Cu_2(OH)_3NO_3 + 3HNO_3$$

This phenomenon has already been observed and used by Huang *et al.* to synthesize $Cu_2(OH)_3NO_3$ on ZIF-8@AGF (activated graphene fiber). This composite also demonstrated great potential as a sensitive cancer cell detection probe for the early diagnosis and management of various cancer diseases.[43] ZIF-8 is a zinc-based MOF, like CALF-20, which suggests that zinc has a major role in the $Cu_2(OH)_3NO_3$ formation.

A similar behavior can be observed in the FTIR spectra (Fig. 5d), where the spectrum of the sample before ion removal from aqueous solution (yellow curve) presents peaks related to PAN (pink curve) and CALF-20 (black curve), without the presence of new peaks or absence of pre-existing peaks, indicating that there is no formation or breaking of bonds. In contrast, as seen in the XRD results, new peaks are observed both for the sample after Pb(II) removal and for the sample after Cu(II) removal. After Pb(II) removal, the peaks are at 520, 772, 1560 and 1610 cm^{-1}. For Cu(II) removal, the peak is at 1109 cm^{-1}. Besides that, the peak related to C–N in the triazole ring at 1320 cm^{-1}, present in the spectrum of the as-spun sample, reduced significantly after ion removal.

From the full XPS spectra (Fig. 5e) before and after metal removal, it is possible to observe the presence of C, N, O and Zn in all cases. However, following Cu(II) removal, peaks related to Cu 2p and Cu 3s are present and after Pb(II) removal, peaks related to Pb 5p, Pb 4d, and Pb 3d can be observed. This analysis confirms the presence of the metal on the mats after removal.

3.3 Removal kinetics and isotherms

The plots and model data are shown in Fig. 6 and Table 2, respectively. Although adsorption isotherms and kinetic models were applied for data fitting, the morphological analyses reveals that the primary removal mechanism is not adsorption but precipitation, driven by physicochemical interactions between the metal ions and the PAN + CALF-20 membrane. The experimental kinetics of Pb(II) and Cu(II) removal were compared with the PFO and PSO models and are presented in Fig. 6a and b, where it is possible to observe that in both cases there is a good correlation with the PFO model, particularly at early stages, suggesting that the rate-limiting step involves diffusion or interfacial nucleation rather than chemisorption. The R^2 for each system was 0.999 and 0.985 for Pb(II) and Cu(II) removal, respectively. For Pb(II) removal, the PFO model values were: $q_e = 196.7$ mg g^{-1} and $K_1 = 0.01879$ min^{-1}, while for Cu(II) removal the model values were $q_e = 106.4$ and $K_1 = 0.02324$ min^{-1}. Although the PSO model also provides reasonable fits, its application here should be regarded as empirical, as its underlying assumptions are associated with adsorption-controlled processes and do not reflect the precipitation-driven removal mechanism observed experimentally.

For Pb(II), a rapid uptake is observed in the first 120 minutes, reaching equilibrium at approximately 240 minutes. This suggests that the rate-limiting step is more consistent with mass transport or nucleation-controlled precipitation rather than chemisorption. Post-treatment SEM images of the membrane surface showed the formation of two-dimensional hexagonal plate-like crystals, indicative of a precipitation-driven mechanism, possibly involving lead hydroxide or lead carbonate derivatives formed under localized basic conditions facilitated by the membrane, this process, however, is accompanied by partial MOF structural decay. Cu(II) removal followed a similar kinetic trend, reaching equilibrium more quickly (in 180 minutes), and the formation of bipyramidal crystalline particles after treatment further rules out adsorption as the dominant mechanism and confirms that nucleation and crystal growth control Cu(II) removal, likely influenced again by local pH changes or coordination with CALF-20 and/or PAN functional groups.

The equilibrium adsorption data, modeled using Langmuir, Freundlich, and Temkin isotherms, are shown in Fig. 6c and d. For Pb(II), the data closely follow the Langmuir model ($R^2 = 0.998$). Despite the excellent fit, applying the Langmuir model does not imply monolayer adsorption in this system, as the observed saturation behavior is more accurately explained by precipitation saturation and surface-limited crystal growth. The uniform morphology of the hexagonal platelets observed in the SEM images reinforces this interpretation. The Langmuir model provides values of $q_m = 552.7$ mg g^{-1} and $K_L = 0.0137$ L mg^{-1} for Pb(II).

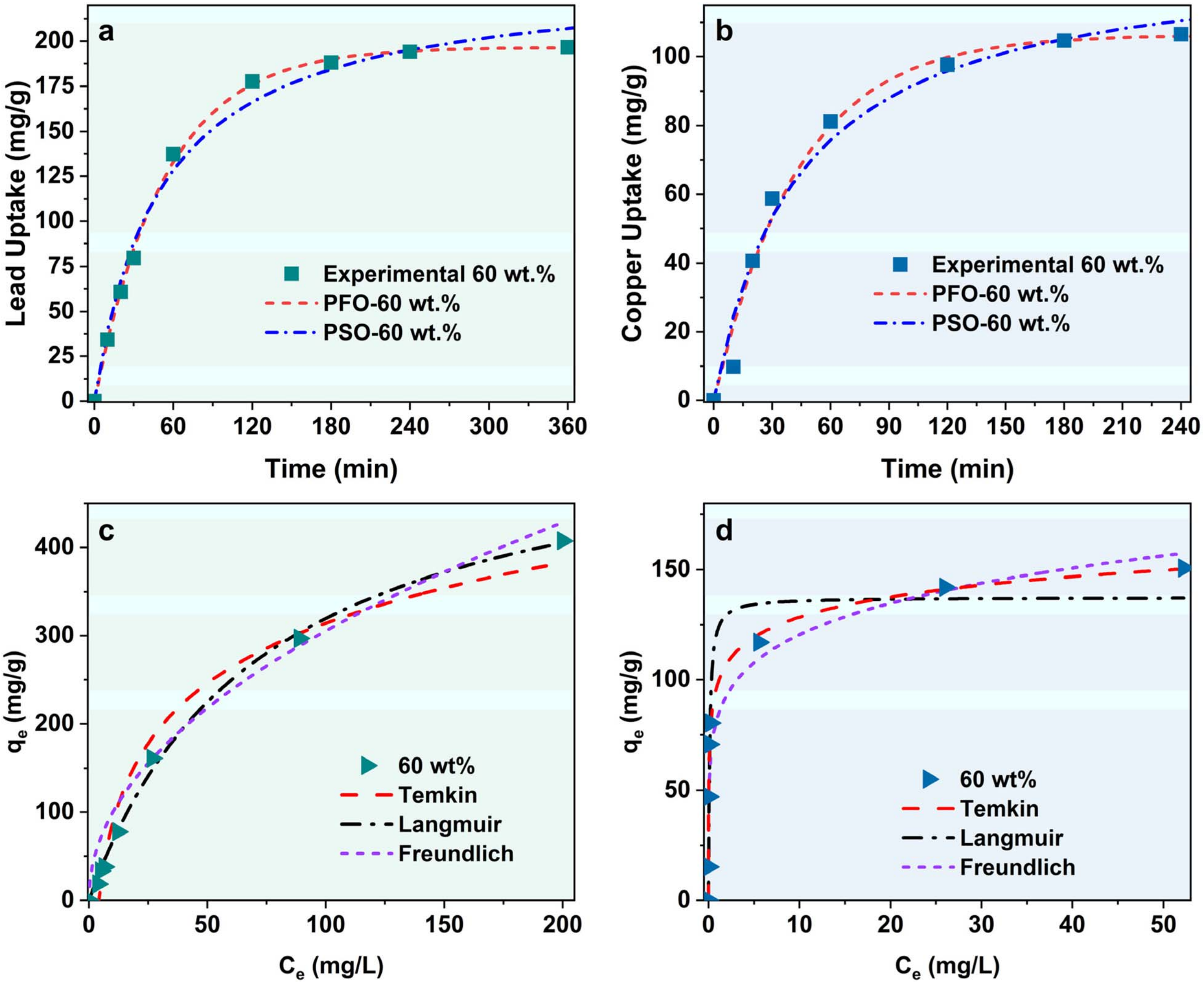

Fig. 6 Experimental kinetics of CALF-20 (60 wt%) + PAN membranes: (a) Pb(II) and (b) Cu(II) removal, compared with pseudo-first order and pseudo-second order models. Experimental isotherms of CALF-20 (60 wt%) + PAN membranes: (c) Pb(II) and (d) Cu(II), compared with the Temkin, Langmuir and Freundlich models.

Table 2 Data of kinetic models for Cu(II) and Pb(II) removal of CALF-20 (60 wt%) + PAN membranes

	PFO	PSO
Lead		
q_e [mg g^{-1}]	196.7	235.9
K [min^{-1}]	0.01879	0.00008
R^2	0.999	0.990
Copper		
q_e [mg g^{-1}]	106.4	130.3
K [min^{-1}]	0.02324	0.00018
R^2	0.985	0.976

In contrast, Cu(II) isotherm data align better with the Freundlich and Temkin models, suggesting a heterogeneous precipitation process facilitated by the membrane surface, rather than adsorption on energetically distinct sites. Overall, the kinetic and equilibrium modeling results must be interpreted with caution, as classical adsorption models do not mechanistically describe precipitation-driven metal removal in the PAN + CALF-20 membrane system.

Despite their limited mechanistic applicability to precipitation-dominated systems, the PFO and PSO kinetic models, as well as the Langmuir, Freundlich, and Temkin isotherm models, were employed strictly as empirical and comparative tools. Their use is justified because they provide a convenient and widely recognized framework to describe time-dependent removal and equilibrium behavior, enabling a consistent quantitative analysis of the experimental data. Moreover, the application of these models allows direct comparison with adsorption-based materials and membrane systems reported in the literature, where such kinetic and isothermal formalisms are routinely used, even when removal mechanisms are complex or mixed. Accordingly, the parameters derived from these models should be interpreted only as descriptive indicators of removal trends and saturation behavior, and not as mechanistic evidence of adsorption, surface-site control, or chemisorption. In the present system, the kinetic and equilibrium fits primarily reflect precipitation kinetics, surface-facilitated nucleation, and precipitation saturation, rather than classical adsorption phenomena.

3.4 Influence of pH

The pH plays a major role in the heavy metal removal for any system. In this work the range of pH was chosen to be between 3 and 6.5 because copper and lead nitrates precipitate under basic conditions and CALF-20 can be seriously damaged under low pH. Fig. 7 shows the removal efficiency of Cu(II) and Pb(II) under different pHs, it also shows the zinc leakage after removal under the respective pHs. For both copper and lead the removal efficiency is the highest at pH 3, however, the zinc leakage is the highest at this condition. This result indicates that the removal mechanism under acidic conditions is ion exchange, instead of precipitation or adsorption, *i.e.*, the zinc atoms are replaced by copper or lead, forming a new compound. This phenomenon was observed by Y. Zhang *et al.*, they observed that ZIF-8, a zinc-based MOF, shows a high Cu(II) adsorption capacity and suggested that the ion exchange mechanism was the best one to explain the obtained results, the reasons for it are: the similar atomic radius of Zn and Cu, and the chemical coordination ability of Cu(II) is stronger than Zn(II) because the valence electron layer structure of Zn(II) is more stable than Cu(II).[44,45] At higher pHs the removal efficiency increases because the ion exchange mechanism is replaced by the induced local pH change (in the case of copper removal), caused by the membrane composite.

Regarding the Zn leaching it is not only an indication of CALF-20 degradation, but also an environmental concern. Although there is no health-based guideline for zinc in drinking water, its release into water can be a problem only when it happens in high levels, altering the color and taste of water, and once discharged into soil can reduce soil fertility by disrupting nutrient balance and impairing the growth of plants.[6,46]

In the case that only two removal mechanisms occur in these systems—ion exchange and precipitation—the contribution of each can be quantified by correlating metal removal (Cu(II) or Pb(II)) with zinc leaching into the solution. In the precipitation mechanism, copper or lead ions form insoluble species without releasing zinc into the aqueous phase. On the other hand, ion exchange involves the substitution of Zn(II) ions in the MOF structure by the target metal ions, resulting in measurable zinc release; therefore, zinc leaching can be directly associated with the ion exchange process.

As shown in Fig. S9, ion exchange is favored at lower pH for both copper and lead removal, although its contribution is markedly higher for copper. Specifically, ion exchange accounts for approximately 99% of Cu(II) removal at pH 3, decreasing to about 4% at pH 6.5. In contrast, Pb(II) removal *via* ion exchange contributes around 24% at pH 3 and only 2% at pH 6.5. Notably, a lower contribution of ion exchange does not imply the retention of zinc within the MOF structure, as released Zn(II) ions may subsequently participate in the formation of lead-based precipitates.

3.5 Influence of initial concentration and membrane dosage

To find the best parameters for the removal of the metals under study, an analysis was carried out on the influence of the membrane dosage (amount of mass of mat in 100 mL of aqueous solution) and initial concentration of the metals on the removal efficiency (*R*%). Fig. 8 illustrates the surface plots for the removal efficiency of Pb(II) and Cu(II) as a function of initial metal ion concentration (55–200 mg L^{-1}) and membrane dosage (0.5–1.5 g L^{-1}). The removal efficiency is represented using a color gradient, ranging from low (blue) to high (red) values, with maximum of 100%.

For Pb(II) (Fig. 8a), the removal efficiency remains consistently high (*R*% > 90%) at lower initial concentrations (55–100 mg L^{-1}) across all membrane dosages. However, at higher concentrations (>130 mg L^{-1}), a notable decline in removal is observed, especially at lower mat loadings (PAN + CALF-20 (60%)), showing that the initial concentration of Pb(II) has a major influence on the removal, while the amount of mat is less important. This trend suggests that the removal system

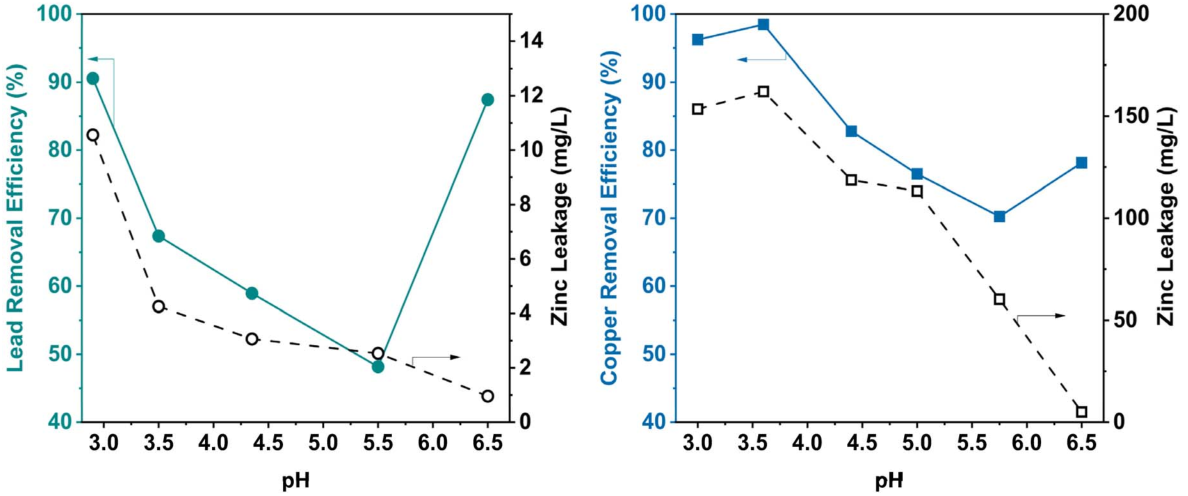

Fig. 7 Influence of pH on: (left) lead removal efficiency and zinc leakage and (right) copper removal efficiency and zinc leakage (CALF-20 (60 wt%) + PAN membranes, 4 hours of removal and C_0 155 mg L^{-1}).

becomes progressively saturated as Pb(II) concentration increases, leading to reduced performance unless membrane dosage is sufficiently increased.

In contrast, Cu(II) (Fig. 8b) exhibits a stronger dependency on adsorbent loading. At low membrane doses (<0.8 g L^{-1}), removal efficiency is significantly limited ($R\% < 65\%$), regardless of initial concentration. As the adsorbent loading increases beyond 1.0 g L^{-1}, removal performance improves sharply, reaching $R\%$ values above 95% at the highest loading levels. This behavior indicates that Cu(II) removal is more dependent on surface area or binding site availability. This occurs because the particles formed during the removal process are connected to the surface of PAN fibers, which means that increasing the fiber loading not only increases the amount of CALF-20 but also increases the area available for the growth of copper-based particles.

These results highlight the differing adsorption behaviors of the two metal ions by PAN + CALF-20 electrospun mats, with Pb(II) demonstrating effective removal at moderate membrane dosages and low metal initial concentrations, while Cu(II) requires a higher quantity of adsorbent to achieve similar performance. This distinction is critical for designing efficient adsorption-based water treatment systems targeting multiple heavy metals.

Based on these results, the systems with highest q_t and $R\% > 95\%$ are chosen as best for ion removal. For Pb(II) the best condition was $C_0 = 130$ mg L^{-1}, 0.5 g L^{-1} for the loading of mat, and 6 h for removal time, leading to a $q_t = 248.3$ mg g^{-1} and $R\% = 95.5\%$. For Cu(II) the chosen condition was $C_0 = 200$ mg L^{-1}, 1.5 g L^{-1} for the loading of mat, and 4 h for removal time, leading to a $q_t = 128.2$ mg g^{-1} and $R\% = 96.2\%$.

The influence of membrane dosage was evaluated in the removal of Cu(II) and Pb(II) in a multicomponent system with five metal ions, including Pb(II), Cu(II), Cr(III), Fe(III), and Ni(II), using a simulated real coal mine wastewater condition.[47] The results, Fig. 9, show that the removal efficiency is high for all the ions when using a membrane dosage from 0.5 to 1.5 g L^{-1}, indicating that an efficient removal can be achieved even at low dosages of membrane. Although the removal efficiency of Pb(II) is slightly reduced (≈85%), when compared with the single component system, the removal efficiency is high for all the other ions (>99 for Cu(II) and Fe(III) and >94% for Cr and Ni). These results indicate that there is no selectivity during the removal process.

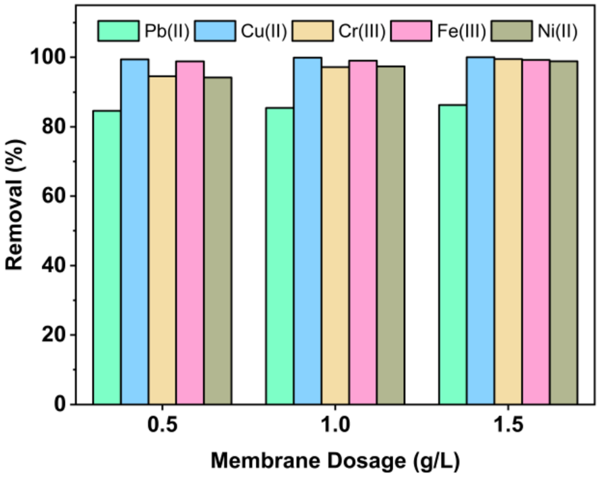

Fig. 9 Removal efficiency of Pb(II), Cu(II), Cr(III), Fe(III), and Ni(II) from a multi-component system using different dosages of CALF-20 (60 wt%) + PAN fibers.

Table 3 shows that the performance of PAN + CALF-20 nanofibers surpasses most previously reported electrospun MOF systems in terms of adsorption capacity, and efficiency. Many earlier studies use low MOF contents (5–20 wt%) to maintain fiber quality, which often limits removal capacity. CALF-20 can be incorporated at a much higher loading (60 wt%) in PAN nanofibers, which increases the number of available active sites and leads to high removal efficiencies above 95% for both Pb(II) and Cu(II). However, such a high MOF content may raise concerns about material cost and long-term mechanical

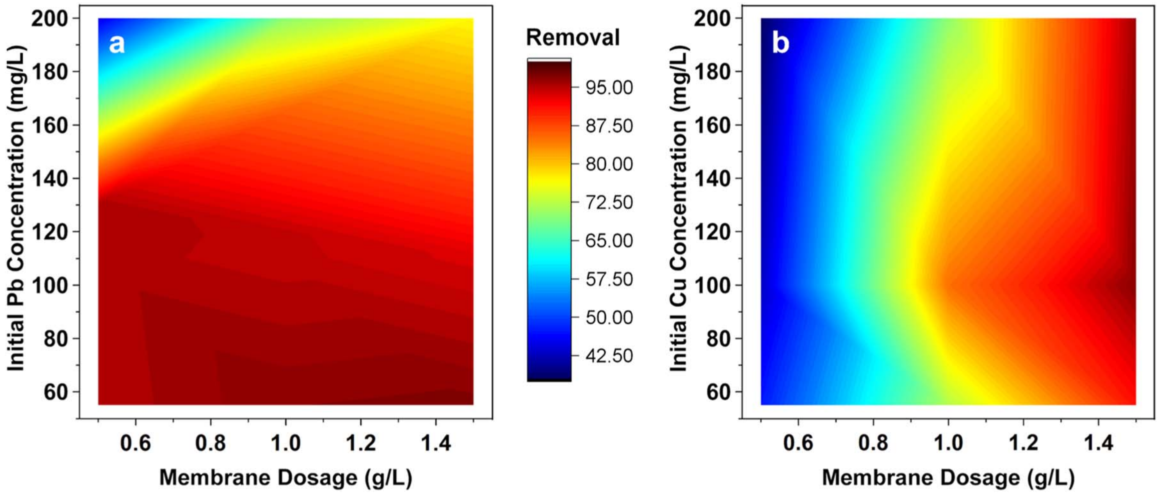

Fig. 8 Influence of the initial metal concentration and membrane dosage (CALF-20 (60 wt%) + PAN) on the removal efficiency of (a) Pb(II) and (b) Cu(II).

Table 3 Data comparison of works using electrospun fibers and MOFs for heavy metal removal

MOF	MOF content [wt%]	Polymer	Ion	C_0 [mg L^{-1}]	Membrane dosage [g L^{-1}]	R [%]	q_t [mg g^{-1}]	Time [h]	Reference
ZIF-8	5	PAN/PEI	Cr(IV)	50	0.20	—	161.55	16	48
MOF-808-EDTA	37.5	PAN	Cu(II)	200	—	97.7	≈60	2	49
UiO-66-NH$_2$	5	CE/CH	Cu(II)	50	—	≈90	≈50	6	50
ZIF-67	20	PVA	Pb(II)	50	0.02	—	140.3	2	51
UiO-66-NH$_2$	15	PAN/PAMAM	Pb(II)	200	0.50	—	56	2	52
UiO-66(COOH)$_2$	5	PVC	Pb(II)	50	3.33	>90	≈15	1	53
In situ ZIF-8	50	PAN	U(VI)	100	0.60	—	≈90	2	54
ZIF-94	8	PAN	Co(II)	70	0.02	—	94.97	12.5	55
CALF-20	60	PAN	Pb(II)	130	0.50	95.5	248.3	6	This work
CALF-20	60	PAN	Cu(II)	200	1.50	96.2	128.2	4	This work

stability compared to lower-loading systems, as observed in Fig. 3.

In terms of removal capacity, CALF-20 shows a clear advantage over most reported systems. For Pb(II), it reaches 248.3 mg g^{-1}, which is significantly higher than values reported for ZIF-8, ZIF-67, ZIF-94, and UiO-66–based membranes under similar conditions. Importantly, for Cu(II), CALF-20 also exhibits a substantially higher removal capacity (>128.2 mg g^{-1}) compared to MOF-808-EDTA and UiO-66-NH$_2$ membranes, which typically show capacities around 60 mg g^{-1}, despite being designed to enhance metal binding.[49,50]

Regarding kinetics, CALF-20 requires 4–6 h to reach high removal efficiency, which can be considered relatively long compared to some systems that achieve similar performance within 1–2 h. At the same time, several reported membranes, such as ZIF-8 and ZIF-94 composites, require much longer contact times (up to 12–16 h),[48,55] placing CALF-20 in an intermediate range rather than at the slow end. Importantly, the CALF-20 membranes are tested at higher membrane loadings and higher initial metal concentrations, which can partly explain the longer equilibration times.

Overall, CALF-20-based electrospun membranes compare favorably with most reported systems in terms of removal capacity and removal efficiency, especially for Pb(II), while showing reasonable but not exceptional kinetics. These results indicate that CALF-20 is a strong candidate for heavy metal removal, though further optimization aimed at reducing contact time and assessing mechanical durability at high MOF loadings would be beneficial.

4 Conclusions

This study introduces, for the first time, the Zn-based MOF, CALF-20, in electrospun nanofiber composites for water treatment applications. The successful integration of CALF-20 into polyacrylonitrile (PAN) fibers *via* direct electrospinning overcomes the limitations of MOF powders and results in free-standing, mechanically robust mats. Among all formulations studied, mats with 60 wt% CALF-20 offered the best balance between structural integrity and removal performance, achieving high capacities of 248.3 mg g^{-1} for Pb(II) and 128.2 mg g^{-1} for Cu(II). Unlike conventional MOF-based adsorbents, the removal mechanism here is dominated by surface-facilitated precipitation, as supported by morphological and structural evidence, including formation of distinct crystalline phases on the fiber surfaces. Kinetic and isotherm analyses further validated a diffusion-controlled uptake process. These findings not only demonstrate the feasibility of incorporating CALF-20 into nanofiber architectures but also establish a new class of electrospun MOF composites for efficient, scalable, and multifunctional environmental remediation technologies.

Author contributions

Guilherme Henrique Franca Melo: conceptualization, methodology, validation, formal analysis, investigation, data curation, writing—original draft, visualization, project administration. Yuxin Liu:conceptualization, validation, formal analysis, writing—review and editing. Jinfeng Zhang: conceptualization, validation, formal analysis, writing—review and editing. Nicholas Fylstra: validation, formal analysis, writing—review and editing. George Shimizu: validation, formal analysis, resources, writing—review and editing. Uttandaraman Sundararaj: validation, formal analysis, resources, writing—review and editing, supervision, project administration.

Conflicts of interest

The authors declare that they have no conflicts of interest.

Data availability

The data supporting this article have been included as part of the supplementary information (SI). Supplementary information: additional characterization data. See DOI: https://doi.org/10.1039/d5ra09555g.

Acknowledgements

The authors would like to thank Natural Sciences and Engineering Research Council of Canada (NSERC) grant number 2020-04058 for funding and Alberta Innovates for AI Advance Grant 232403381 and for graduate scholarships (GM and YL).

References

1 L. Lin, H. Yang and X. Xu, Effects of Water Pollution on Human Health and Disease Heterogeneity: A Review, *Front. Environ. Sci.*, 2022, **10**, 1–16, DOI: 10.3389/fenvs.2022.880246.

2 L. Schweitzer, J. Noblet, Water Contamination and Pollution, *Green Chemistry*, Elsevier, 2018, pp. 261–290, DOI: 10.1016/B978-0-12-809270-5.00011-X.

3 C. Zamora-Ledezma, D. Negrete-Bolagay, F. Figueroa, E. Zamora-Ledezma, M. Ni, F. Alexis, *et al.*, Heavy metal water pollution: A fresh look about hazards, novel and conventional remediation methods, *Environ. Technol. Innov.*, 2021, **22**, 101504, DOI: 10.1016/j.eti.2021.101504.

4 S. Landsberger, F. Iskander, S. Basunia, D. Barnes and M. Kaminski, Lead and copper contamination of soil from industrial activities and firing ranges, *Biol. Trace Elem. Res.*, 1999, **71–72**, 387–396, DOI: 10.1007/BF02784226.

5 World Health Organization, Lead in drinking-water Health risks, monitoring and corrective actions, Technical brief, 2022.

6 World Health Organization, Guidelines for Drinking-water Quality fourth edition incorporating the first addendum, 2017.

7 S. Wei, E. Berti, D. Ma, Q. Wu, Y. Peng, C. Yuan, *et al.*, Global patterns and drivers of lead concentration in inland waters, *J. Hazard. Mater.*, 2023, **460**, 132455, DOI: 10.1016/j.jhazmat.2023.132455.

8 Agency for Toxic Substances and Disease Registry, Public health statement copper, 2004.

9 N. A. A. Qasem, R. H. Mohammed and D. U. Lawal, Removal of heavy metal ions from wastewater: a comprehensive and critical review, *npj Clean Water*, 2021, **4**, 36, DOI: 10.1038/s41545-021-00127-0.

10 F. Fu and Q. Wang, Removal of heavy metal ions from wastewaters: A review, *J. Environ. Manage.*, 2011, **92**, 407–418, DOI: 10.1016/j.jenvman.2010.11.011.

11 F. Zadehahmadi, N. T. Eden, H. Mahdavi, K. Konstas, J. I. Mardel, M. Shaibani, *et al.*, Removal of metals from water using MOF-based composite adsorbents, *Environ. Sci.*, 2023, **9**, 1305–1330, DOI: 10.1039/D2EW00941B.

12 G. Wu, J. Ma, S. Li, J. Li, X. Wang and Z. Zhang, Functional metal–organic frameworks as adsorbents used for water decontamination: design strategies and applications, *J. Mater. Chem. A*, 2023, **11**, 6747–6771, DOI: 10.1039/D3TA00279A.

13 The Royal Swedish Academy of Sciences, Nobel Prize in Chemistry 2025, 2025.

14 V. F. Yusuf, N. I. Malek and S. K. Kailasa, Review on Metal–Organic Framework Classification, Synthetic Approaches, and Influencing Factors: Applications in Energy, Drug Delivery, and Wastewater Treatment, *ACS Omega*, 2022, **7**, 44507–44531, DOI: 10.1021/acsomega.2c05310.

15 P. S. Abhari, F. Manteghi and Z. Tehrani, Adsorption of Lead Ions by a Green AC/HKUST-1 Nanocomposite, *Nanomaterials*, 2020, **10**, 1647, DOI: 10.3390/nano10091647.

16 Y. Wang, M. Li, J. Hu, W. Feng, J. Li and Z. You, Highly efficient and selective removal of Pb2+ by ultrafast synthesis of HKUST-1: Kinetic, isotherms and mechanism analysis, *Colloids Surf. A Physicochem. Eng. Asp.*, 2022, **633**, 127852, DOI: 10.1016/j.colsurfa.2021.127852.

17 E. Tahmasebi, M. Y. Masoomi, Y. Yamini and A. Morsali, Application of Mechanosynthesized Azine-Decorated Zinc(II) Metal–Organic Frameworks for Highly Efficient Removal and Extraction of Some HeavJ. Mater. Chem. Ay-Metal Ions from Aqueous Samples: A Comparative Study, *Inorg. Chem.*, 2015, **54**, 425–433, DOI: 10.1021/ic5015384.

18 Y. Huang, X. Zeng, L. Guo, J. Lan, L. Zhang and D. Cao, Heavy metal ion removal of wastewater by zeolite-imidazolate frameworks, *Sep. Purif. Technol.*, 2018, **194**, 462–469, DOI: 10.1016/j.seppur.2017.11.068.

19 Y. Lu, C. Liu, C. Mei, J. Sun, J. Lee, Q. Wu, *et al.*, Recent advances in metal organic framework and cellulose nanomaterial composites, *Coord. Chem. Rev.*, 2022, **461**, 214496, DOI: 10.1016/j.ccr.2022.214496.

20 G. Shimizu, R. Vaidhyanathan, S. Iremonger, K. Deakin, J.-B. Lin and K. W. Dawson, Metal organic framework, production and use thereof cross reference to related applications, *WO Pat.*, WO2014138878A1, 2014.

21 J.-B. Lin, T. T. T. Nguyen, R. Vaidhyanathan, J. Burner, J. M. Taylor, H. Durekova, *et al.*, A scalable metal-organic framework as a durable physisorbent for carbon dioxide capture, *Science*, 2021, **374**, 1464–1469, DOI: 10.1126/science.abi7281.

22 Z. Chen, X. Yang and R. Wang, Engineering metal-organic frameworks via diverse shaping methods for enhanced sorption-based applications, *Matter*, 2025, **8**, 102369, DOI: 10.1016/j.matt.2025.102369.

23 G. W. Peterson, D. T. Lee, H. F. Barton, T. H. Epps and G. N. Parsons, Fibre-based composites from the integration of metal–organic frameworks and polymers, *Nat. Rev. Mater.*, 2021, **6**, 605–621, DOI: 10.1038/s41578-021-00291-2.

24 M. Sedighi, M. J. Azarhoosh, H. Alamgholiloo and N. N. Pesyan, Engineering CALF-20/graphene oxide nanocomposites for enhancing CO2/N2 capture performance, *Process Saf. Environ. Prot.*, 2024, **190**, 1481–1493, DOI: 10.1016/j.psep.2024.08.005.

25 W. Y. Hong, S. P. Perera and A. D. Burrows, Comparison of MIL-101(Cr) metal-organic framework and 13X zeolite monoliths for CO2 capture, *Microporous Mesoporous Mater.*, 2020, **308**, 110525, DOI: 10.1016/j.micromeso.2020.110525.

26 H. I. Adil, M. R. Thalji, S. A. Yasin, I. A. Saeed, M. A. Assiri, K. F. Chong, *et al.*, Metal–organic frameworks (MOFs) based nanofiber architectures for the removal of heavy metal ions, *RSC Adv.*, 2022, **12**, 1433–1450, DOI: 10.1039/D1RA07034G.

27 J. E. Efome, D. Rana, T. Matsuura and C. Q. Lan, Metal–organic frameworks supported on nanofibers to remove heavy metals, *J. Mater. Chem. A*, 2018, **6**, 4550–4555, DOI: 10.1039/C7TA10428F.

28 P. Kampalanonwat and P. Supaphol, Preparation and Adsorption Behavior of Aminated Electrospun Polyacrylonitrile Nanofiber Mats for Heavy Metal Ion

Removal, *ACS Appl. Mater. Interfaces*, 2010, **2**, 3619–3627, DOI: 10.1021/am1008024.

29 F. Zhu, Y.-M. Zheng, B.-G. Zhang and Y.-R. Dai, A critical review on the electrospun nanofibrous membranes for the adsorption of heavy metals in water treatment, *J. Hazard. Mater.*, 2021, **401**, 123608, DOI: 10.1016/j.jhazmat.2020.123608.

30 J. M. Taylor, R. K. Mah, G. K. H. Shimizu. Synthesis of zinc MOF materials. *US Pat.*, US11230562B2, 2022.

31 A. Awad, Removal efficiency, metal uptake, and breakthrough curve of aqueous lead ions removal using olive stone waste, *Results Eng.*, 2024, **22**, 102311, DOI: 10.1016/j.rineng.2024.102311.

32 E. D. Revellame, D. L. Fortela, W. Sharp, R. Hernandez and M. E. Zappi, Adsorption kinetic modeling using pseudo-first order and pseudo-second order rate laws: A review, *Clean Eng. Technol.*, 2020, **1**, 100032, DOI: 10.1016/j.clet.2020.100032.

33 I. Langmuir, THE ADSORPTION OF GASES ON PLANE SURFACES OF GLASS, MICA AND PLATINUM, *J. Am. Chem. Soc.*, 1918, **40**, 1361–1403, DOI: 10.1021/ja02242a004.

34 H. Freundlich, Of the adsorption of gases. Section II. Kinetics and energetics of gas adsorption. Introductory paper to section II, *Trans. Faraday Soc.*, 1932, **28**, 195, DOI: 10.1039/tf9322800195.

35 M. I. Temkin, Adsorption equilibrium and the kinetics of processes on nonhomogeneous surfaces and in the interaction between adsorbed molecules, *Russ. J. Phys. Chem.*, 1941, **15**, 296–332.

36 Test Method for Tensile Properties of Plastics2014. doi: DOI: 10.1520/D0638-14.

37 M. Thommes, K. Kaneko, A. V. Neimark, J. P. Olivier, F. Rodriguez-Reinoso, J. Rouquerol, *et al.*, Physisorption of gases, with special reference to the evaluation of surface area and pore size distribution (IUPAC Technical Report), *Pure Appl. Chem.*, 2015, **87**, 1051–1069, DOI: 10.1515/pac-2014-1117.

38 R. Oktavian, R. Goeminne, L. T. Glasby, P. Song, R. Huynh, O. T. Qazvini, *et al.*, Gas adsorption and framework flexibility of CALF-20 explored via experiments and simulations, *Nat. Commun.*, 2024, **15**, 3898, DOI: 10.1038/s41467-024-48136-0.

39 W. Wang, Y. Wang, R. He, X. Wang, Z. Shen, X. Han, *et al.*, Ultrafast Single-Crystal-to-Single-Crystal Transformation from Metal–Organic Framework to 2D Hydroxide, *Adv. Mater.*, 2022, **34**, 2106400, DOI: 10.1002/adma.202106400.

40 J. Drwęska, F. Formalik, K. Roztocki, R. Q. Snurr, L. J. Barbour and A. M. Janiak, Unveiling Temperature-Induced Structural Phase Transformations and CO 2 Binding Sites in CALF-20, *Inorg. Chem.*, 2024, **63**, 19277–19286, DOI: 10.1021/acs.inorgchem.4c02952.

41 R. Marangoni, R. E. Carvalho, M. V. Machado, V. B. Dos Santos, S. Saba, G. V. Botteselle, *et al.*, Layered Copper Hydroxide Salts as Catalyst for the "Click" Reaction and Their Application in Methyl Orange Photocatalytic Discoloration, *Catalysts*, 2023, **13**, 426, DOI: 10.3390/catal13020426.

42 M. Rezvani Jalal, H. Hojjati, J. Rezvani Jalal, S. Ebrahimi and M. R. Zangene Bighashi, Growth of $$\hbox {Ag}_{2}\hbox {O}_{2}$$ micro-particles and $$\hbox {Cu}_{2}(\hbox {OH})_{3}\hbox {NO}_{3}$$ nano-sheets by atmospheric pin-to-solution electrical discharge, *Bull. Mater. Sci.*, 2020, **43**, 105, DOI: 10.1007/s12034-020-2071-2.

43 W. Huang, Y. Xu and Y. Sun, Functionalized Graphene Fiber Modified With MOF-Derived Rime-Like Hierarchical Nanozyme for Electrochemical Biosensing of H2O2 in Cancer Cells, *Front. Chem.*, 2022, **10**, 873287, DOI: 10.3389/fchem.2022.873187.

44 Y. Zhang, Z. Xie, Z. Wang, X. Feng, Y. Wang and A. Wu, Unveiling the adsorption mechanism of zeolitic imidazolate framework-8 with high efficiency for removal of copper ions from aqueous solutions, *Dalton Trans.*, 2016, **45**, 12653–12660, DOI: 10.1039/C6DT01827K.

45 V. V. S. Mummidivarapu, S. Bandaru, D. S. Yarramala, K. Samanta, D. S. Mhatre and C. P. Rao, Binding and Ratiometric Dual Ion Recognition of Zn 2+ and Cu 2+ by 1,3,5-Tris-amidoquinoline Conjugate of Calix[6]arene by Spectroscopy and Its Supramolecular Features by Microscopy, *Anal. Chem.*, 2015, **87**, 4988–4995, DOI: 10.1021/acs.analchem.5b00905.

46 H.-T. Van, V. H. Hoang, L. T. Q. Nga and V. Q. Nguyen, Effects of Zn pollution on soil: Pollution sources, impacts and solutions, *Results Surf. Interfaces*, 2024, **17**, 100360, DOI: 10.1016/j.rsurfi.2024.100360.

47 G. Bi, X. Li, X. Du, X. Sun and W. Yao, Remediation of Heavy Metal Pollution from Coal Mine Effluent Using Metal-Organic Frameworks (MOF): Impact of Water Media, Operational Factors and Metal Characteristics, *Minerals*, 2024, **14**, 764, DOI: 10.3390/min14080764.

48 Y. A. Y. A. Mohammed, A. M. Abdel-Mohsen, Q.-J. Zhang, M. Younas, L.-B. Zhong, J.-C. E. Yang, *et al.*, Facile synthesis of ZIF-8 incorporated electrospun PAN/PEI nanofibrous composite membrane for efficient Cr(VI) adsorption from water, *Chem. Eng. J.*, 2023, **461**, 141972, DOI: 10.1016/j.cej.2023.141972.

49 X. Chen, D. Chen, N. Li, Q. Xu, H. Li, J. He, *et al.*, Modified-MOF-808-Loaded Polyacrylonitrile Membrane for Highly Efficient, Simultaneous Emulsion Separation and Heavy Metal Ion Removal, *ACS Appl. Mater. Interfaces*, 2020, **12**, 39227–39235, DOI: 10.1021/acsami.0c10290.

50 R. Luo, K. Zhang, Y. Qin, L. Xie, X. Chai, L. Zhang, *et al.*, Amine-functionalized UiO-66 incorporated electrospun cellulose/chitosan porous nanofibrous membranes for removing copper ions, *Chem. Eng. J.*, 2024, **480**, 148077, DOI: 10.1016/j.cej.2023.148077.

51 S. Singh, N. Pavithra, B. Uppara, R. Varshney, N. Shehata, N. A. Khan, J. Joji, J. Singh, P. C. Ramamurthy, *et al.*, Facile Synthesis of ZIF-67-Incorporated Electrospun PVA Nanofibers Composite for Efficient Pb (II) Adsorption from Water: Docking and Experimental Studies, *ACS ES&T Water*, 2024, 4497–4509, DOI: 10.1021/acsestwater.4c00500.

52 X. Wang, D. Zhang, Z. Ji, Y. Xu, Y. Zhao and M. Xie, Facile fabrication of PAN/PAMAM@UiO-66-NH2 composite nanofiber membranes for enhanced Pb2+ adsorption, *J.*

Water Proc. Eng., 2025, **71**, 107022, DOI: 10.1016/j.jwpe.2025.107022.

53 M. H. Hashem, M. Hammoud, M. N. Ahmad and M. Hmadeh, Electrospun Polyvinyl Chloride/UiO-66(COOH) 2 Nanocomposite Membranes for Efficient and Rapid Heavy Metal Removal, *ACS Appl. Mater. Interfaces*, 2025, **17**, 16275–16286, DOI: 10.1021/acsami.4c22963.

54 C. Wang, T. Zheng, R. Luo, C. Liu, M. Zhang, J. Li, *et al.*, In Situ Growth of ZIF-8 on PAN Fibrous Filters for Highly Efficient U(VI) Removal, *ACS Appl. Mater. Interfaces*, 2018, **10**, 24164–24171, DOI: 10.1021/acsami.8b07826.

55 C. Yin, Y. Peng, H. Li, G. Yang and G. Yuan, Facile construction of ZIF-94/PAN nanofiber by electrospinning for the removal of Co(II) from wastewater, *Sci. Rep.*, 2024, **14**, 414, DOI: 10.1038/s41598-023-50796-9.